

# Photoluminescence Dynamics Defined by Exciton Trapping Potential of Coupled Defect States in DNA-Functionalized Carbon Nanotubes

Yu Zheng,\* Braden M. Weight, Andrew C. Jones, Vigneshwaran Chandrasekaran, Brendan J. Gifford, Sergei Tretiak, Stephen K. Doorn, and Han Htoon\*



Cite This: *ACS Nano* 2021, 15, 923–933



Read Online

ACCESS |



Metrics & More



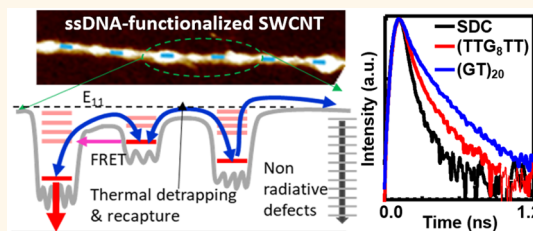
Article Recommendations



Supporting Information

**ABSTRACT:** Chemical reactions between semiconducting single-wall carbon nanotubes (SWCNTs) and single-stranded DNA (ssDNA) achieve spatially patterned covalent functionalization sites and create coupled fluorescent quantum defects on the nanotube surface, tailoring SWCNT photophysics for applications such as single-photon emitters in quantum information technologies. The evaluation of relaxation dynamics of photoluminescence (PL) from those coupled quantum defects is essential for understanding the nanotube electronic structure and beneficial to the design of quantum light emitters. Here, we measured the PL decay for ssDNA-functionalized SWCNTs as a function of the guanine content of the ssDNA oligo that dictates the red-shifting of their PL emission peaks relative to the band-edge exciton. We then correlate the observed dependence of PL decay dynamics on energy red-shifts to the exciton potential energy landscape, which is modeled using first-principles approaches based upon the morphology of ssDNA-altered SWCNTs obtained by atomic force microscopy (AFM) imaging. Our simulations illustrate that the multiple guanine defects introduced within a single ssDNA strand strongly interact to create a deep exciton trapping well, acting as a single hybrid trap. The emission decay from the distinctive trapping potential landscape is found to be biexponential for ssDNA-modified SWCNTs. We attributed the fast time component of the biexponential PL decay to the redistribution of exciton population among the lowest energy bright states and a manifold of dark states emerging from the coupling of multiple guanine defects. The long lifetime component in the biexponential decay, on the other hand, is attributed to the redistribution of exciton population among different exciton trapping sites that arise from the binding of multiple ssDNA strands along the nanotube axis. AFM measurements indicate that those trapping sites are separated on average by  $\sim 8$  nm along the nanotube axis.

**KEYWORDS:** photoluminescence relaxation, exciton localization, patterned quantum defects, coupled trapping potential wells, J-aggregates, exciton hopping process



Enhancing the versatility of structure-specific photoluminescence for semiconducting single-wall carbon nanotubes (SWCNTs) through the intentional introduction of quantum defects in the nanotube sidewall has attracted significant interest. This synthetic route offers flexible modifications of SWCNT electronic and optical properties and advances the prospects for their applications as quantum light emitters.<sup>1–6</sup> Chemical methods of oxygen doping and aryl group functionalization create sparse fluorescent quantum defects at random positions on the nanotube surface, causing local perturbations of SWCNT  $\pi$ -electron systems and leading to local band gap changes that can trap diffusive band-edge  $E_{11}$  excitons.<sup>7–10</sup> The localization of excitons at defect sites in such

chemically altered nanotubes enhances fluorescence quantum yield and causes spectrally red-shifted photoluminescence, leading to advanced SWCNT photonic functionality, improved image contrast in biological tissues, and the realization of room-temperature single-photon emission at telecom wavelengths.<sup>5,7,9,11–14</sup>

**Received:** September 7, 2020

**Accepted:** December 29, 2020

**Published:** January 4, 2021



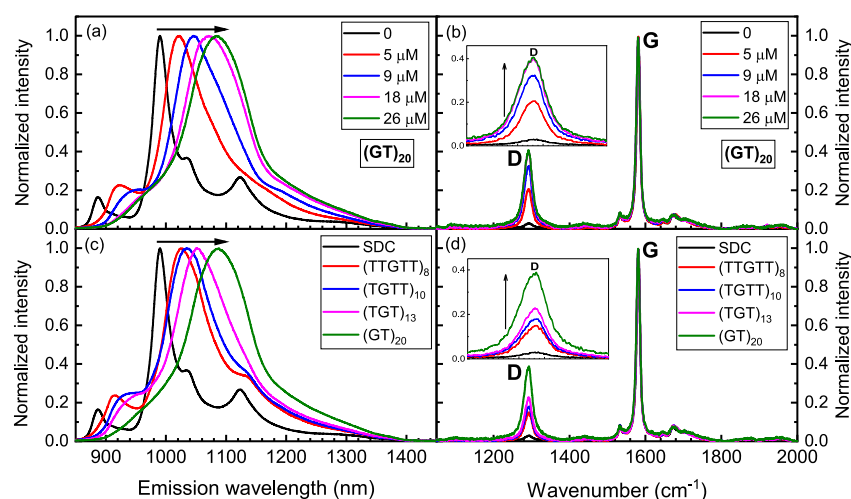


**Figure 1.** (a) Fluorescence spectra (excitation wavelength at 570 nm) of samples of SWCNTs dispersed with  $(GT)_{20}$  ssDNA after the treatment with different amounts of rose bengal concentrations including 0, 5, 9, 18, and 26  $\mu\text{M}$ . The black arrow indicates the spectral redshifts with the increased rose bengal concentration. (b) Raman spectra of SWCNT samples obtained in (a). The black arrow illustrates an enhanced D phonon band with the increased rose bengal concentration. (c) Fluorescence spectra of samples of SWCNTs dispersed with  $(TTGTT)_8$ ,  $(TGTT)_{10}$ ,  $(TGT)_{13}$ , and  $(GT)_{20}$  ssDNA oligos before and after the treatment. The black curve represents emission before the treatment. The singlet oxygen doses are sufficient to reach the maximum spectral shift for those ssDNA oligos. (d) Raman spectra of SWCNT samples obtained in (c).

The recent discovery of chemical reactions between SWCNT sidewalls and guanine nucleotides in single-stranded DNA (ssDNA) coatings on exposure to singlet ( $^1\Delta_g$ ) oxygen reveals a different approach for implantation of defects to the nanotube surface.<sup>15–19</sup> Singlet oxygen ( $^1\text{O}_2$ ) exclusively reacts with guanine nucleobases in the ssDNA coatings, producing reactive guanine endoperoxide that can be covalently attached to the SWCNT sidewall.<sup>19</sup> Each reacted guanine defect causes a local perturbation to the nanotube electronic structure and leads to a shallow trapping potential well that affects exciton diffusion on the nanotube surface. The helical wrapping of ssDNA oligos around SWCNT surfaces allows the introduction of periodically distributed fluorescent quantum guanine defects in the nanotube sidewall. The spatial density of patterned defects and thus the exciton trapping potentials in the nanotube sidewall can be easily controlled by experimental conditions (e.g.,  $^1\text{O}_2$  dose) and guanine content in ssDNA coatings, achieving smooth modulation of nanotube electronic energy levels and leading to tunable spectrally shifted photoluminescence.<sup>19</sup>

The advanced prospects for emerging photonic functionalities of chemically modified SWCNTs, in which the diffusive band-edge excitons can be localized at the trapping sites, motivate intense efforts toward understanding relaxation dynamics of defect-state photoluminescence to aid in the design of altered nanotubes for specific performance.<sup>20–25</sup> The relaxation of the defect-state emission (denoted  $E_{11}^*$ ) for aryl-functionalized SWCNTs has shown that the defect-state PL lifetime increases as the nanotube diameter decreases.<sup>24</sup> This result suggests that the primary nonradiative relaxation process is multiple phonon decay (MPD), whose rate decreases as more quanta of phonons are required to match the nanotube energy gap.<sup>26</sup> The phonon-assisted thermal detrapping of defect-state excitons is another important channel for the loss of defect-state population for single nanotube chiralities, causing increased PL lifetime with increasing emission wavelengths.<sup>25</sup> The defect-state emission from sparsely functionalized SWCNTs displays a biexponential decay, arising

from energetically close bright and dark states within the defect-state manifold. The short decay component has been assigned as the redistribution of exciton population between bright and dark defect states, whereas the long lifetime component is the characteristic time for the entire defect-state manifold decaying back to the ground state.<sup>24,25</sup> Unlike the sparse covalent functionalization of SWCNTs that leads to the spectrally shifted defect-state emission feature ( $E_{11}^*$ ) well-separated from the pristine emission ( $E_{11}$ ), ssDNA-altered SWCNTs create multiple defect states along the nanotube axis with trapping depths that are defined by ssDNA sequences, giving smooth red-shifting of the  $E_{11}$  emission with no appearance of an additional new peak.<sup>19</sup> The significantly different modulation of nanotube electronic structures for DNA functionalization from oxygen and aryl doping could lead to previously inaccessible quantum mechanical coupling of defect states in the ssDNA-modified nanotube. A comprehensive understanding on how the distinct exciton potential landscape of ssDNA-functionalized SWCNTs dictates their PL relaxation dynamics is essential for developing advanced applications in quantum photonics, quantum computing, and quantum cryptography. With this motivation, we performed measurements of solution-phase photoluminescence dynamics for samples of SWCNTs functionalized by different ssDNA sequences with guanine content varying from 0 to 50%. The experimental findings are then correlated with the morphology of ssDNA-SWCNTs, and the formation of a distinctive confinement potential landscape is revealed by atomic force microscopy (AFM) studies and first-principles simulations.

## RESULTS AND DISCUSSION

**Tunable Defect-State Photoluminescence Spectra.** In samples of SWCNTs suspended in ssDNA oligos, a chemical reaction between the nanotube sidewall and guanine nucleotides proceeds quickly at room temperature in the presence of  $^1\text{O}_2$ , which is formed through optical irradiation of a rose bengal sensitizer.<sup>27</sup> We prepared samples of CoMoCAT SWCNTs suspended in a variety of ssDNA oligos and then

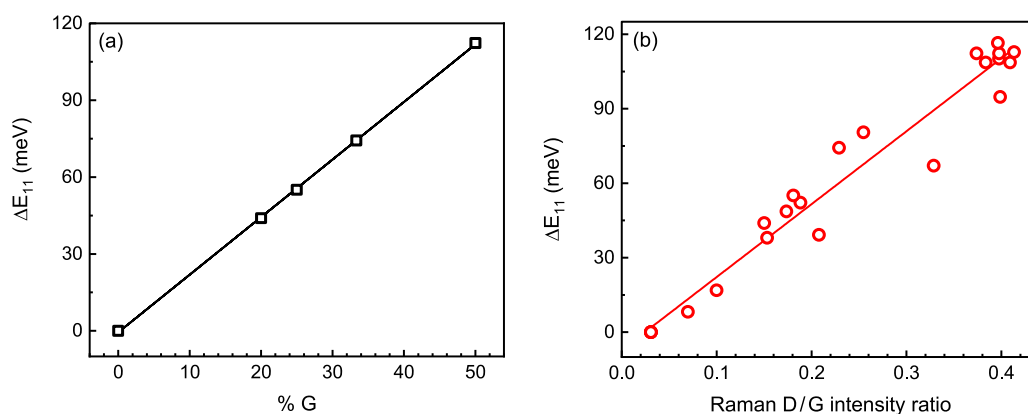


**Figure 2.** (a) Plot of the final spectral shift of  $E_{11}$  emission as a function of the guanine content in ssDNA coatings. The shifts were obtained with maximum singlet oxygen doses. (b) Plot of the spectral shift of  $E_{11}$  emission against intensity ratio of the Raman D/G band. Data were obtained with different ssDNA oligos and different singlet oxygen doses.

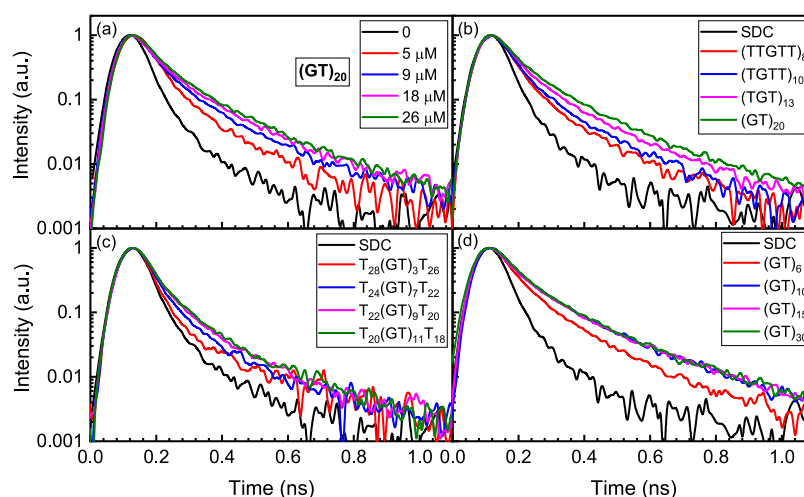


**Figure 3.** Photoluminescence dynamics (excitation wavelength at 840 nm) of different SWCNT samples. (a) SWCNTs were dispersed in  $(GT)_{20}$  solutions and treated with different amounts of rose bengal concentrations including 0, 5, 9, 18, and 26  $\mu\text{M}$ . (b) The black curve shows the PL dynamics for the sample before the treatment. Other curves represent the relaxation for samples of SWCNTs dispersed in solutions of  $(TTGTT)_8$ ,  $(TGTT)_{10}$ ,  $(TGT)_{13}$ , and  $(GT)_{20}$  ssDNA and treated with maximum singlet oxygen doses. (c) Samples of SWCNTs were treated with  $T_{28}(GT)_3T_{26}$ ,  $T_{24}(GT)_7T_{22}$ ,  $T_{22}(GT)_9T_{20}$ , and  $T_{20}(GT)_{11}T_{18}$  ssDNA oligos. (d) Samples of SWCNTs were treated with  $(GT)_6$ ,  $(GT)_{10}$ ,  $(GT)_{15}$ , and  $(GT)_{30}$  ssDNA oligos.

treated with  $^1\text{O}_2$ . The treated SWCNT samples were redispersed in a solution of 1% (w/v) sodium deoxycholate (SDC), which is known as a strong surfactant to individualize nanotubes, through 100 K membrane filtration to remove any noncovalently bonded ssDNA and residual rose bengal.<sup>28</sup>

Samples of SWCNTs were dispersed and chemically functionalized with a variety of ssDNA sequences including  $(TTGTT)_8$ ,  $(TGTT)_{10}$ ,  $(TGT)_{13}$ ,  $(GT)_{20}$ ,  $(GT)_6$ ,  $(GT)_{10}$ ,  $(GT)_{15}$ ,  $(GT)_{30}$ ,  $T_{28}(GT)_3T_{26}$ ,  $T_{26}(GT)_5T_{24}$ ,  $T_{24}(GT)_7T_{22}$ ,  $T_{22}(GT)_9T_{20}$ , and  $T_{20}(GT)_{11}T_{18}$ . Figure 1a shows the fluorescence spectra of the treated samples in  $(GT)_{20}$  ssDNA as a function of the concentration of rose bengal, which is known as a singlet oxygen sensitizer.<sup>27</sup> The red-shift of the treated emission peak (denoted as  $E_{11}^*$ ) grows monotonically with a concomitant increase in  $^1\text{O}_2$  dose, approaching an asymptotic value, accompanied by a gradual enhancement of Raman D/G band intensity ratio from 0.03 to 0.41, indicating the increasing conversion of  $sp^2$ -hybridized carbon lattice to  $sp^3$  fluorescent defects (see Figures 1b and S1).<sup>29–31</sup> The distinct spectral transformation was observed for SWCNTs functionalized with several ssDNA oligos that contain different

amounts of guanine nucleotides (see Figures 1c and S2). The final spectral shifts (denoted as  $\Delta E_{11}$ ) are directly proportional to the fraction of guanine nucleotides in the ssDNA coating, as shown in Figure 2a. The value of  $\Delta E_{11}$  for (6, 5) SWCNTs increases from 0 to ca. 110 meV as the guanine content increases from 0 to 50%. The ssDNA oligo that lacks guanine bases has no chemical reaction with SWCNT sidewalls and thus can be removed by SDC through the surfactant exchange process. The enhanced guanine fraction in the ssDNA oligo introduces an increasing amount of  $sp^3$  defects in the nanotube sidewall, illustrated by the enhanced Raman D/G intensity ratio in Figure 1d. A plot of the spectral shift against Raman D/G intensity ratio obtained with different ssDNA oligos and different  $^1\text{O}_2$  doses, as shown in Figure 2b, indicates that the spectral shifts increase nearly proportionally to the SWCNT defect density. These results together provide a clear evidence that the defect-emission band can be tuned smoothly by controlling the covalent binding of guanine nucleotides through the concentration of  $^1\text{O}_2$  sensitizer (rose bengal) and the guanine content of the ssDNA strand.

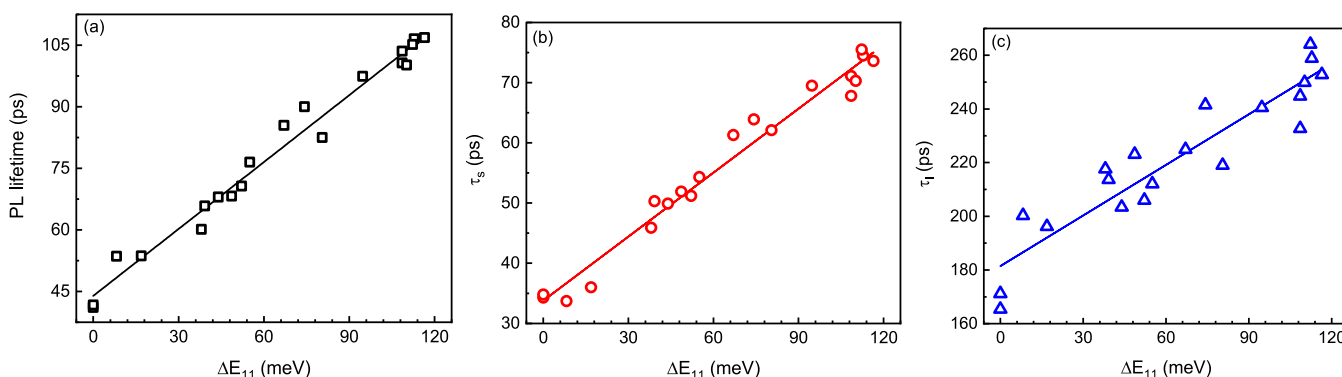


**Figure 4.** Plots of (a) average photoluminescence lifetime (black square symbol), (b) short lifetime component (red circle), and (c) long lifetime component (blue triangle) as a function of spectral shift of  $E_{11}$  emission.

This behavior stands in contrast with previously reported findings for oxygen-, aryl-, or alkyl-functionalized SWCNTs, where the increase in defect density only leads to the strengthening of defect emission at a fixed spectral position accompanied by a gradual disappearance of pristine  $E_{11}$  emission.<sup>7–10</sup> This difference stems directly from the fact that defects randomly introduced by those prior functionalization approaches remain isolated from one another even at extremely high dopant concentration, whereas the DNA functionalization could implant guanine defects in SWCNTs in a tight spatial pattern with a separation of  $\sim 1$ – $2$  nm. At low rose bengal concentration or low guanine content, relatively isolated guanine defects were formed with a shallow trapping potential reflected by the less than 50 meV red-shift from pristine emission (see Figure 1a,c). When rose bengal concentration or guanine content increases, more guanine defects are created with separations close enough to strongly couple and to form a cumulative trapping potential that is deepened with enhanced defect density. The defect emission as a result becomes continuously tunable. Our AFM and theoretical modeling presented in the following sections further support this explanation.

**Controllable Defect-State Photoluminescence Dynamics.** We measured photoluminescence dynamics for samples of SWCNTs treated with different ssDNA oligos, as shown in Figure 3. For a given  $(GT)_{20}$  ssDNA, the PL decay time becomes longer with increasing the dose of  $^1O_2$ , arising from more reacted guanine defects in the nanotube sidewall (see Figure 3a). The relaxation dynamics of the final spectrally shifted emission for SWCNTs were also varied with different ssDNA sequences. As plotted in Figure 3b,c, the PL decay lifetime increases monotonically with enhanced guanine content in ssDNA oligos. An increased fraction of G bases allows more closely and densely patterned fluorescent defects in the nanotube sidewall, intensifying the perturbation of the nanotube electronic structure and thus leading to the increased lifetime for the relaxation of the treated nanotube emission. We also studied the ssDNA length effect on the defect-state emission properties. Similar spectral shifts and PL dynamics were observed for SWCNTs functionalized with  $(GT)_{10}$ ,  $(GT)_{15}$ ,  $(GT)_{20}$ , and  $(GT)_{30}$  oligos (see Figures 3d and S3, S4), whereas the  $(GT)_6$ -modified nanotube gives a smaller spectral shift and a faster decay of the treated emission as compared to longer  $(GT)_n$  ssDNA oligos ( $n$  is a positive integer). We suspect that the  $(GT)_6$  sequence is too short to allow efficient wrapping around SWCNT surfaces, leading to a relatively loose guanine pattern in the nanotube. The “tandem”

ssDNA sequences with the pattern of  $T_{31-n}(GT)_nT_{29-n}$  contain a segment of 50% guanine and two tail segments that lack guanine bases, showing a faster PL relaxation than that in the  $(GT)_{30}$  oligo (see Figures 3c and S5, S6). The thymine fragments in oligos of  $T_{31-n}(GT)_nT_{29-n}$  should be protected from the chemical reaction with  $^1O_2$  and therefore preserve the pristine nanotube segment, whereas the  $(GT)_n$  fragment provides functionalization sites every two nucleotides and thus leads to modification of the nanotube segment.<sup>32</sup> Therefore, the tandem ssDNA causes less alteration of the entire nanotube electronic structure and leads to overall smaller cumulative exciton trapping potential along the nanotube axis as compared to  $(GT)_{30}$ -patterned SWCNTs. The smooth modification of SWCNT energy levels through ssDNA-templated covalent functionalization provides a route to control SWCNT photoluminescence dynamics.

#### Dependence of Photoluminescence Lifetime on $\Delta E_{11}$ .

The PL relaxation dynamics of samples of SWCNTs treated with ssDNA display a biexponential decay that has been observed in sparsely aryl-functionalized nanotubes,<sup>24</sup> despite the periodically distributed fluorescent defects in the sidewall of the DNA-altered nanotube. The biexponential decay shows a short lifetime component ( $\tau_s$ ) on time scales of tens of ps and a long lifetime component ( $\tau_l$ ) with decay times of hundreds of ps (see Figure S7). In the biexponential relaxation process, the short component has been assigned as the characteristic time for the exciton redistribution across bright and dark states associated with the defect site, whereas the slow decay corresponds to the relaxation of the excited state back to the ground state.<sup>24,25</sup> As we have discussed above, the PL relaxation dynamics for single-chirality nanotubes are varied with different ssDNA compositions, accompanied by changes in the spectrally shifted emission feature. The PL decay lifetime is plotted as a function of the spectral shift of the treated emission from the  $E_{11}$  band-edge (see Figures 4 and S8). The results clearly show increased PL lifetime correlated with increased spectral shifts. The average lifetime of the biexponential relaxation increases by a factor of  $\sim 2.5$  when the treated emission feature is red-shifted by  $\sim 110$  meV (see Figure 4a). Such robust dependence of the PL dynamics on the spectral shift originates from the strong effects of  $\Delta E_{11}$  on both the fast and slow decay processes, as illustrated in Figure 4b,c. The short and long lifetime components strongly depend on the spectral red-shift with an approximately linear relationship.

This behavior stands in contrast with that observed previously in aryl-functionalized SWCNTs, where only the long component of the PL decay was reported to increase with

longer emission wavelength.<sup>25</sup> Multiple nonradiative decay processes, including multiphonon decay (MPD), electronic to vibrational energy transfer (EVET), where excitons undergo Förster resonance energy transfer (FRET) to the near-infrared vibration modes of solvents, and thermal detrapping of the defect-bound exciton followed by recombination at non-radiative defects, have been assigned as key channels defining the PL decay dynamic of aryl-doped SWCNTs.<sup>24,25</sup> Among those processes, MPD requires PL decay to slow down with the increase in PL emission energy ( $E_{\text{PL}}$ ), which is opposite to the trend reported in Figure 4, *i.e.*, slow-down of PL decay with enhanced energy red-shift ( $\Delta E_{11} = E_{11} - E_{\text{PL}}$ ).<sup>24</sup> Given that the ssDNA wrapping could also shield defect-bound excitons from efficiently coupling with solvent phonons, EVET is also expected to be more than 1 order of magnitude slower than the observed dynamics (see details in the Supporting Information).

Thermal detrapping followed by recombination at non-radiative defects successfully explains the observed positive correlation between long decay components and emission wavelengths in aryl-functionalized SWCNTs.<sup>25</sup> For ssDNA-functionalized SWCNTs with the trapping potential barrier ( $E_a$ ) defined by a 110 meV energy red-shift, the Arrhenius relation  $1/\tau_{\text{dt}} = Ae^{-E_a/k_B T}$  yields the phonon-assisted detrapping time  $\tau_{\text{dt}}$  to be on the order of  $\sim 10$  ps, which is an order of magnitude faster than the observed long lifetime in Figure 4. Although this detrapping time could only be taken as a qualitative estimate due to the exponential sensitivity of the detrapping rate on  $E_a$ , a significant disagreement with the observed value suggests that the DNA covalent functionalization somehow slows down the thermal detrapping process.

We hypothesize that this significant modification in the dynamics of the exciton detrapping process, as well as the observed strong dependence of PL dynamics on spectral shifts (see Figure 4), is derived from the distinct potential landscape of individual trapping sites and interactions between trapping sites created by different ssDNA strands. Specifically, when multiple ssDNA strands are helically wrapped around individual SWCNTs and then covalently bound to the nanotube surface through the  $^1\text{O}_2$ -induced chemical reaction, a series of trapping sites is formed along the length of the nanotube. Excitons in oxygen- or aryl-functionalized nanotubes, in contrast, see mostly a flat potential landscape of the  $E_{11}$  band edge that is interspersed with isolated localized deep trapping potentials at the sparsely implanted defect sites. We believe that this difference in potential landscapes gives rise to the distinct electronic structure and trapping/detrapping mechanisms that in turn lead to the observed PL decay dynamics. To investigate this hypothesis, we determined the spatial distribution of ssDNA strands along the nanotube axis through AFM measurements and then performed density functional theory (DFT) simulations to study interactions of multiple covalent defects placed within single ssDNA strands and coupling of multiple defect states from different ssDNA strands, thus revealing the distinct potential landscape in the nanotube sidewall.

**Structure of ssDNA-SWCNTs Revealed by AFM.** The ssDNA-SWCNT samples were spin-coated on freshly cleaved mica substrates for characterization using AFM. As shown in Figure 5, the helical wrapping of (GT)<sub>20</sub> ssDNA on SWCNT surfaces persists after the sample was exchanged to SDC surfactant and washed with deionized water three times through 100 K membrane filtration, indicating that DNA

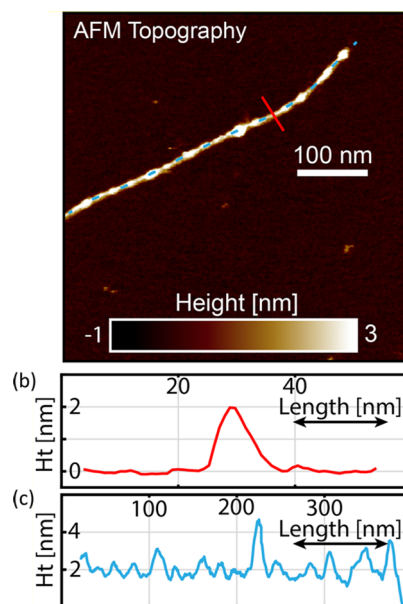


**Figure 5.** In-fluid AFM characterization: (a) AFM topography image of a single SWCNT covalently functionalized with (GT)<sub>20</sub> oligos. (b) Cross-sectional line-cut measurement of the ssDNA-SWCNT diameter in the position highlighted with the red line in (a). (c) Line trace along the nanotube axis.

oligos have been covalently bound to the nanotube surface. We performed AFM imaging in a liquid water environment to better visualize topographic variations within the (GT)<sub>20</sub> ssDNA-wrapped nanotubes.<sup>33–35</sup> The AFM topography of a typical ssDNA-SWCNT hybrid is shown in Figure 5 and exhibits a mean diameter of  $2.1 \pm 0.4$  nm. Here, we observed nanometer-scale height modulations along the nanotube axis, which we attribute to the variation in the wrappings of individual ssDNA strands. The average length of those height modulations, depicted by the line trace in Figure 5c, was found to be  $12.8 \pm 2.5$  nm, while the spacing between consecutive height modulations (center to center distance) is found to be  $20 \pm 4$  nm.

The total ssDNA length ( $L$ ), the helical wrapping pitch ( $h$ ), the number of turns around the nanotube cylinder ( $n$ ), and the diameter of the ssDNA-SWCNT hybrid ( $d$ ) can be calculated when the values of three of these parameters are given.<sup>34</sup> Compensating for the thickness of ssDNA ( $d_{\text{DNA}}$ ), one turn of ssDNA wrapped around a nanotube can be formed by rolling a rectangle with lengths equal to  $h$  and  $d - d_{\text{DNA}}$  so the following equation is obtained:  $L = n\sqrt{h^2 + (\pi(d - d_{\text{DNA}}))^2}$ .<sup>34</sup> As the (GT)<sub>20</sub> ssDNA contains 40 nucleobases and the average linear nucleobase spacing in ssDNA is 0.676 nm,<sup>36</sup> the total length  $L$  is defined as  $\sim 27$  nm. According to the AFM results, we can experimentally relate the measured diameter  $d$  to the diameters of the nanotube,  $d_{\text{CNT}}$ , and DNA using the relation  $d = d_{\text{CNT}} + 2d_{\text{DNA}}$ . Under the interpretation that the product of  $n$  and  $h$  represents the length of a wrapped segment of the nanotube and that this length corresponds to 12.8 nm modulations observed along the nanotube axis ( $nh = 12.8$  nm), we are able to express the equation above for the total length of the ssDNA strand in terms of  $h$  and numerically solve to determine the helical pitch. Here, we estimate that the (GT)<sub>20</sub> ssDNA are wrapped around the nanotube surface with a helical pitch of  $h = 2.4_{-1.1}^{+1.5}$  nm, which corresponds to  $n = 5.4_{+2.2}^{-1.5}$  turns around the

nanotube. These measured parameters are consistent with the findings of ssDNA-SWCNT structures through molecular dynamics simulations, which report a  $\sim 2$  nm helical pitch for (GT)<sub>30</sub> ssDNA.<sup>37,38</sup> These results further yield that the axial separation between guanine nucleotides in (GT)<sub>n</sub> ( $n$  is a positive integer) can be smaller than 1.0 nm. With an average distance between sequential height modulations of  $\sim 20$  nm, we estimate the end-to-end spatial distance between adjacent helically wrapped ssDNA to be  $\sim 8$  nm. The above analysis is based upon the perfect helical wrapping of ssDNA on SWCNT surfaces, but we think that locally disrupted helices and other distorted configurations should exist in experimentally prepared samples.<sup>38</sup>

**DFT Modeling of Coupled Defects.** In samples of SWCNTs covalently functionalized with ssDNA, multiple guanine defects within one ssDNA strand are so closely patterned along the nanotube axis that the excitonic wave functions associated with each defect, which typically remain delocalized by *ca.* 2–5 nm along the nanotube axis,<sup>39</sup> become strongly overlapping and interacting. Under the interpretation that raised sections along the nanotube axis represent tightly bound ssDNA, the AFM studies indicate that groups of defects in adjacent ssDNA strands are separated on average by *ca.* 8 nm. We performed quantum chemistry simulations to understand the interactions of defects spatially patterned on these two different length scales. Because a large size of the DNA strand containing guanine nucleotides prevents us from determining exact chemical binding configurations through realistic simulations, we have formulated our theoretical model by applying the previous quantum-chemical insights attained on the aryl defects<sup>40,41</sup> to the defect separation within a single DNA strand as well as between different strands.

Specifically our previous experiment–theory correlated studies have shown that  $sp^3$  defects can be created with chemical binding configurations denoted as ortho  $-$ ,  $+$ , and  $+$  with energy red-shifts of  $<50$ , 110, and  $>200$  meV, respectively.<sup>40,41</sup> Among these three configurations, the energy red-shift of the ortho  $-$  configuration seems to match with the small energy red-shift observed for isolated guanine defects at low rose bengal concentration and at low guanine content. However, we cannot make a specific assignment because other nontopological factors such as mono/di/multivalency,  $sp^3$  character (which is always partial), and induction effects could also strongly influence energy red-shift of the defect state.<sup>42,43</sup> Furthermore, because of the shallow trapping potential, such defects have highly delocalized wave function spreading over 10 nm, making the computation expense for simulating coupling of multiple such defects very high. For these reasons we choose the most red-shifted, “ortho  $+$ ” configuration with an exciton wave function spread of  $\sim 2$  nm as the model defect and investigate how the coupling of multiple defects modifies the exciton potential landscape. This choice leads to a significant disagreement between calculated initial red-shift of a single  $sp^3$  defect and the one observed at low rose bengal and low guanine content. However, the calculations allow us to demonstrate that coupling of multiple defects can give rise to a cumulative confinement potential that is continuously tunable with interdefect separation and number of coupled defects. These physical insights are expected to be independent of the initial energy red-shift of isolated defects, as they are controlled solely by the interaction between defects.

We used DFT to optimize the coupled defect geometries and then compute singlet excitations using time-dependent

DFT (TD-DFT) methodology (see Computational Methodology for further computational details). The oscillator strengths for the first two excitonic states and the diagonal extent of the transition density matrix for the lowest energy state are calculated as functions of defect–defect axial separation distance, as illustrated in Figure 6. The transition

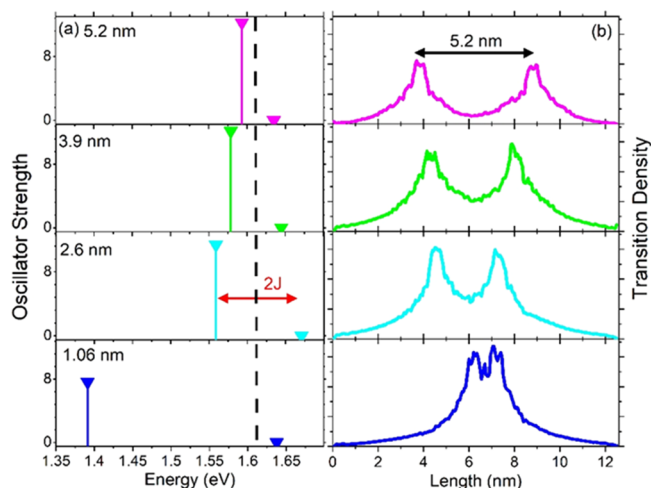


**Figure 6.** (a) Calculated oscillator strength for the first two excitonic states in spatially separated defects as a function of absorption energy. The distances sampled between axially separated  $sp^3$ -hybridized defects includes 1.06, 2.6, 3.9, and 5.2 nm. The absorption energy of a single-defect system is plotted as a dashed black line for reference. (b) Diagonal extent of the transition density matrix of the lowest energy bright exciton for SWCNTs in (a).

density indicates the position of the center of mass of the exciton along the nanotube and thus characterizes the delocalization of its wave function.<sup>39</sup> The geometries were manipulated by changing the axial separation of the two defects from 1.06 to 5.2 nm. The computed absorption energy of a single-defect system is plotted as a dashed black line for reference.

We first consider larger defect separations, where our simulations mimic interactions between two trapping sites formed by two different ssDNA strands. Nearly symmetrical splitting around the single-defect energy of the first and second excitons can be seen in the top three panels of Figure 6a for the interacting defects with large separation ( $r > 2.0$  nm). This is a typical case for a Frenkel exciton system. In such systems, two sites form a Davydov’s pair of excitons whose wave functions represent symmetric and antisymmetric superpositions of the respective single-defect parents.<sup>44</sup> The splitting of each state from the single-defect exciton increases as the interdefect axial separation is reduced, indicating a concomitant strengthening of the interaction between defect sites (see Figure 6a). The values of those interactions, symbolized as  $J$ , are 20.8, 33.1, and 55.9 meV for 5.2, 3.9, and 2.6 nm separations, respectively, as calculated as half of the energy splitting between states. The interactions of the largely spaced ( $r > 2$  nm) interacting defects can be interpreted as an electrostatic interaction between transition dipole moments of individual excitons at defect sites. For any given geometric arrangement of defects, the resulting transition dipoles are oriented in parallel along the SWCNT axis, leading to a case similar to molecular J-aggregates. In this case, the transition dipoles align “head-to-tail” as in the Kasha

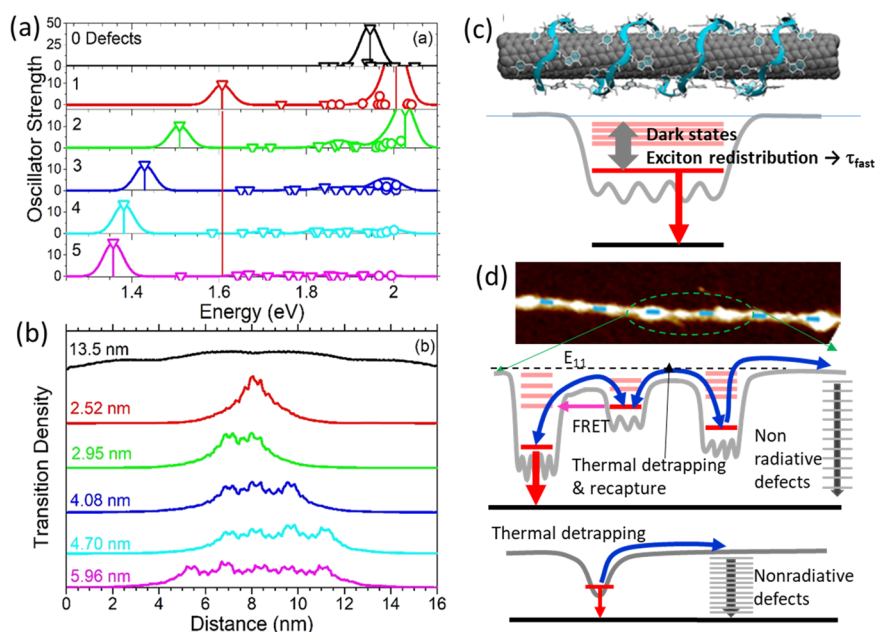


**Figure 7.** (a) Oscillator strength for six computed geometries with increasing defect concentration from 0 to 5  $sp^3$ -hybridized defects, each of which is spaced at a fixed distance of 1.3 nm along the nanotube axis. Increased red-shifts of the lowest energy bright state are observed with the increased number of defects placed on the nanotube surface. The symbol of the oscillator strength shows the type of exciton: defect-associated (triangles) and pristine-associated (circles). (b) Absolute values of diagonal elements of the normalized transition density matrix of the lowest energy bright state, which are vertically offset and colored to match with their counterpart in (a). The participation ratio ( $L_d$ ) for each system is shown. (c) Molecular dynamics snapshot of a single (GT)<sub>20</sub>-wrapped (6, 5) SWCNT. The multiple guanine defects within the single ssDNA form a deep trapping potential well. The bright and dark states are energetically split within the defect-state manifold. Exciton population redistributes within those states (attributed to the fast component  $\tau_{fast}$  of the PL biexponential decay) and then radiatively decays back to the ground state or nonradiatively recombines. (d) AFM image illustrating multiple ssDNA strands wrapped around a single nanotube. The inhomogeneous wrapping of ssDNA strands may cause different trapping potential wells along the nanotube axis. The coupled trapping sites allow the trapping site-to-site exciton hopping and FRET processes. As for sparsely altered SWCNTs (e.g., oxygen and aryl functionalization), the thermal detrapping is the primary nonradiative channel of the loss of exciton in the isolated trapping site.

model,<sup>45–47</sup> where the lowest excitonic state is a symmetric combination that acquires all the oscillator strength, whereas the upper state remains optically forbidden, as illustrated in Figure 6.

The decreased spacing between defects with the axial distance smaller than 2 nm is the opposite limit of our simulations and shows significantly different trends from largely spaced defects ( $r > 2$  nm). Those separations with  $r \leq 1.06$  nm mimic closely spaced guanine defect sites within a single ssDNA strand. Although we still have a pair of states for a system with two individual defects, the splitting between them dramatically increases (bottom panel of Figure 6a). Notably, the splitting of the small separations ( $r < 2$  nm) is no longer symmetric with respect to the single-defect system (black dashed line). Instead, there is a significant asymmetry where the lower energy exciton is further red-shifted and the other one is only slightly affected. The transition density (Figure 6b) of the well-separated defects suggests a large potential energy barrier between their respective potential wells, which can be assumed by the lack of density at the midpoint between the defects as the wave function falls off exponentially. On the other hand, for closely spaced defects (bottom panel of Figure 6b), the “independent” wave functions largely overlap due to the reduction of the energy barrier between them. These observations signify the fact that closely patterned defects ( $r < 2$  nm) form a single, extended, and deep trapping potential well, as is the case for adjacent guanine functionalization sites within single ssDNA strands

where the spacing is  $\leq 1$  nm. The oscillator strengths in those interacting defect geometries, represented by the height of the lines in Figure 6a, are significant for the lower energy exciton, whereas they are always zero for the higher energy exciton. We suspect that this trend will hold for most experimental geometries where adjacent defects are spaced a few carbon rings away in any direction as long as the local SWCNT geometric/ $\pi$ -orbital stability is not infringed upon.

To further understand defect interactions within single ssDNA strands, we computed geometries with increasing defect concentration from 0 to 5 defects, each of which is spaced at a fixed distance of 1.3 nm along the nanotube axis (see Figure S9). The spatial distance of adjacent defects was chosen to represent the upper length boundary such that we still have formation of a single trapping site due to closely spaced defect binding. As illustrated in Figure 7a, the spectral red-shifts of the lowest energy bright exciton become larger as an increased number of defects is placed on the nanotube surface. Although the computational model can only accommodate five defects due to numerical cost limitation, we expect this trend to continue until the exciton size finds its maximal length within those SWCNT systems (see Figure S11). A more complete depiction of the energy level manifold is plotted in Figure S10. We have also found that the transition dipole moment along the nanotube axis and the oscillator strength for the lowest energy bright exciton have a positive relationship with the number of defects. Such linear dependence of the transition dipole moment suggests that the

equivalent dipole moment for (GT)<sub>20</sub>-functionalized SWCNTs is larger than the single-defect dipole by a factor of 3. The calculations further reveal that coupling of multiple defects introduces higher energy exciton states with vanishing oscillator strength, forming a manifold of dark exciton states (Figures 7a and S12). To confirm that an assembly of closely spaced defects creates a single potential energy well for a trapped exciton, we further analyze the diagonal of the transition density matrix. Figure 7b shows the spatial distribution of diagonal elements of the transition density matrix corresponding to the lowest energy bright state in each system. The six systems (from top-to-bottom: pristine and 1-, 2-, 3-, 4-, 5-defect systems) are shown with vertical shifts. The band gap exciton is delocalized across the entire nanotube segment used for simulation. In contrast to a single defect giving a narrow isolated potential energy well, the trapping potentials are strongly overlapped for closely spaced defects, leading to an extended confinement potential (Figure 7b). The participation ratio ( $L_d$ ), which quantitatively measures the exciton center of mass distribution (*i.e.*, the extent to which the excitation is spread across the nanotube), is further calculated for each system. The exciton extension length increases with more defects placed in the nanotube sidewall, indicating enhanced delocalization of the lower energy excitons with increased number of defects (see Figures 7b and S12, S13).

## CONCLUSIONS

Experimental data corroborated by our calculations altogether provide evidence that the strongly interacting multiple guanine defects within a single ssDNA strand lead to an extended trapping potential well that contains multiple excitonic states, as depicted in Figure 7c. The reduced transition energy of the lowest energy bright exciton with the increased number of defects, as revealed by the TD-DFT simulations, illustrates the gradually progressive red-shifts of E<sub>11</sub> emission with increased singlet oxygen dose and enhanced guanine content in ssDNA coatings, as shown in Figure 2. Here, we note that the number of covalent guanine defects as well as their geometrical arrangement could differ from one ssDNA strand to another due to inhomogeneous wrapping, leading in turn to the inhomogeneity in the effective extension lengths and depths of trapping potential wells along the nanotube axis and thus showing the broadening of ensemble PL spectral lines. While TD-DFT simulations show the increased spectral red-shift with the number of coupled guanine defects increased to 5, a saturation of spectral red-shifts can be observed clearly in Figure 7a, corroborating the observed saturation of PL red-shifts and decay dynamics for SWCNTs functionalized by (GT)<sub>n</sub> oligos with *n* from 10 to 30 (see Figures 3d and S3, S4). We attribute the fast time component of the PL biexponential decay to the redistribution of exciton population between the lowest energy bright exciton and the manifold of dark exciton states that arise from the coupling of multiple guanine defects, as schematically represented in Figure 7c. The increase in the fast decay time with the larger energy red-shifts indicates the increased energy separation between the bright and dark manifold with the enhanced energy red-shift.

On the other hand, the helical wrapping of multiple ssDNA strands on SWCNT surfaces allows numerous patterned trapping potential wells to co-exist in a single nanotube. Such spaced trapping sites are coupled, and excitons are capable of hopping or delocalizing across the collection of trapping sites along the nanotube axis *via* FRET and/or

thermally assisted exciton hopping, as illustrated in Figure 7d (upper panel). The energy barrier of the hopping process for a localized exciton could be lower than that of the thermal detrapping to the band-edge E<sub>11</sub> exciton (*e.g.*, barrier to the middle trap in Figure 7d), causing exciton population to redistribute among neighboring traps and leading to a longer residence time in trapping states. Such a hopping process provides a route to reduce the loss of defect-state exciton population *via* thermal detrapping and gives rise to a PL decay time significantly longer than the 10 ps thermal detrapping time, which is calculated based on the 110 meV potential barrier. Specifically in previously reported oxygen- and aryl-functionalized SWCNTs, a defect-bound exciton that thermally detraps to the band edge would rather recombine through nonradiative defects, as shown in the lower panel of Figure 7d, than be retrapped into nearby sites, as in the upper panel. This analysis therefore leads to the conclusion that concomitant dynamics of detrapping and retrapping of excitons in coupled trapping sites from different DNA strands gives rise to a long residence time for excitons that appears as the long lifetime component of the PL decay in Figure 4c. In this picture, the observed strong positive correlation between the energy red-shifts and the long lifetime components in the biexponential PL dynamics arises from the fact that the increase in depth of exciton trapping potentials leads to the reduced rates of the exciton hopping and thermal detrapping processes.

In summary, we have demonstrated that the defect-state PL emission energy as well as the decay dynamics of modified SWCNTs can be tuned continuously by implanting guanine defects with customized spatial patterns and trapping depths along the nanotube axis using ssDNA as a template. Defect-state PL from such altered nanotubes displays a biexponential decay, in which the short and long lifetime components monotonically increase with enhanced guanine spatial density, accompanied by progressive spectral red-shifting of E<sub>11</sub> emission. Our joint AFM measurements and quantum chemistry simulations revealed that multiple guanine defects within a single ssDNA strand are quantum mechanically coupled to form a single trapping potential whose depth and width increase with the enhanced density of guanine defects. The lowest energy state of those coupled defects is bright, whereas the higher energy states are all optically inactive, thus forming a manifold of dark exciton states. We attributed the short time constant of the biexponential PL decay to the redistribution of exciton population among the bright state and dark manifold. The consecutive wrapping of multiple ssDNA strands along the length of individual SWCNTs, on the other hand, leads to the formation of numerous trapping potentials along the nanotube axis that are coupled *via* dipole–dipole interactions. This enables FRET or thermally activated exciton hopping carrier transfer mechanisms. The redistribution of exciton population among the neighboring trapping sites from different DNA strands in a single nanotube, which reflects a concomitant dynamics of trapping, detrapping, and retrapping of excitons, is responsible for the long time constant of the PL decay. The increased long time constant with the enhanced energy red-shift arises from the slow-down of the exciton hopping and thermal detrapping due to the increased trapping potential depth.

## MATERIALS AND METHODS

**Sample Preparation.** Custom-synthesized single-stranded DNA (ssDNA) was purchased from Integrated DNA Technologies.

Aqueous solutions of ssDNA were prepared in 0.1 M sodium chloride (NaCl) and 0.06 M sodium phosphate buffer (pH = 7.4) with the concentration at 1 mg/mL. Raw CoMoCAT SWCNTs (type SG 65i) were purchased from Sigma-Aldrich and added to the ssDNA solution in a weight ratio of *ca.* 1:4. The mixture was dispersed using tip sonication at an output power of 5 W (Sonics, "Vibracell" model no. CV18, 1/4 in. diameter tip) for 60 active minutes (90 min with duty cycle of 40 s on, 20 s off) while kept in an ice–water bath. The sonicated suspension was then centrifuged for 2 h at 13000g in benchtop centrifugation to remove SWCNT impurities and bundles. The supernatant was collected and diluted with 0.1 M NaCl and 0.06 M phosphate buffer and incubated overnight. A stock solution of rose bengal (Sigma-Aldrich) was prepared at a fixed concentration of 338  $\mu\text{M}$ . An aqueous 1% (w/v) sodium deoxycholate (Sigma-Aldrich) solution was prepared for the use in coating exchange. Nanopure water (18.3 M $\Omega$ -cm) was used for the whole sample preparation process.

**Sample Functionalization.** Optical irradiation of rose bengal sensitizer was used to generate singlet oxygen that is needed to induce the chemical reaction between SWCNT sidewalls and guanine nucleotides in ssDNA coatings. The rose bengal stock solution was added to samples of ssDNA-dispersed SWCNTs. The mixture was then irradiated with a green LED (wavelength around 520–530 nm) at a power of *ca.* 10 W. The irradiation time and the added volume of the rose bengal stock solution were varied to control singlet oxygen doses, thus leading to different extents of SWCNT functionalization. The free ssDNA and rose bengal residual in the treated sample were removed by exchanging with 1% SDC solutions through centrifugal filtration (100 kDa membrane).

**AFM Measurement.** The treated sample was washed with nanopure water through centrifugal filtration (100 kDa membrane) three times to remove any noncovalent bindings on the nanotube surface. Then the sample was spin-coated on freshly cleaved mica substrates for AFM measurements. AFM topographic imaging in a purified liquid H<sub>2</sub>O environment was performed using a Dimension Icon AFM to lift unbound DNA from the sample surface and minimize the contact force between the AFM probe and the DNA-wrapped nanotubes.

**Optical Characterization.** Short-wave infrared fluorescence spectra were measured in quartz cells using a Horiba Nanolog spectrofluorometer with a fixed excitation wavelength at 570 nm. An 800 nm long-pass filter was incorporated in the collection beam path to block excitation light. Raman spectra were obtained by using a Trivista triple spectrometer (Princeton Instruments) with 655 nm laser excitation. A home-built microscope–photoluminescence system was used for PL lifetime measurements. The excitation source is a tunable pulsed Ti:sapphire laser (150 fs pulse width, 90 MHz repetition rate). The excitation light with the wavelength at 840 nm (at the (6, 5) SWCNT phonon sideband) was coupled into an inverted microscope body and focused onto the sample with an infrared objective (Olympus, LCPlan N, 50 $\times$ , NA = 0.65). The emission light passed through a 950 nm long-pass filter and was directed into a superconducting nanowire single-photon detector (Single Quantum Eos 210) via a pellicle beamsplitter (Thorlabs, BP133). Photon detection events were recorded using a HydraHarp 400 (Picoquant) time-correlated single photon-counting electronics. All recorded transients were reconvolution fit to a biexponential decay also considering the corresponding instrument response function.

**Computational Methodology.** Two finite-length (6, 5) SWCNTs of  $\sim$ 12 and 16 nm in length (3 and 4 unit cells, respectively) were constructed and capped with hydrogens to preserve the semi-infinite electronic structure, as done in previous works.<sup>42,48,49</sup> Both of the SWCNTs are of sufficient length to negate obtrusive finite-size effects. A set of –CH<sub>3</sub> (methyl) sp<sup>3</sup>-hybridization defects (*i.e.*, where each defect comprises two covalent attachments on a single carbon ring) are placed onto the surface of the 12-nm-long SWCNT in the ortho + configuration<sup>49</sup> with a variety of defect–defect axial separations, which is used as a parameter, ranging in value from 0.18 to 5.2 nm. The ortho + configuration was chosen to reduce the size of the computational cell, as this configuration is the most

red-shifted and exhibits the most localized low-lying, bright exciton. With the addition of multiple defects of this type, edge effects are minimized. The physics behind the tunable red-shift remains the same, irrespective of the choice of configuration, as the underlying phenomenon we probe in this work is the addition of closely packed defects with strongly overlapping wave functions (*i.e.*, within a single ssDNA oligomer), which can be achieved with any configuration of defect. Five defected systems were constructed on the 16-nm-long SWCNT. The nanotube surfaces were modified with different numbers of defects (ranging from 1 to 5), each of which is spaced at a fixed distance of 1.3 nm along the nanotube axis.

All electronic structure calculations were completed using the Gaussian 16 package at the range-corrected CAM-B3LYP/STO-3G functional and basis, respectively.<sup>50,51</sup> A series of DFT calculations were performed, in a vacuum, to optimize the ground-state geometry.<sup>52</sup> Singlet excitations including the first 15 states were completed at each optimized geometry using the TD-DFT approach using the same functional and basis as that for ground-state calculations.<sup>53</sup> Using the exciton energies and ground- to excited-state oscillator strengths, we then compute the exciton density of states and absorption spectrum for each system.

The transition density matrix  $(\xi_{S_i})_{mn}$  was constructed, with the aid of the Multiwfn package, for the low-energy bright exciton in each system, where  $S_i$  represents the singlet exciton and  $m, n$  are SWCNT-axis cross-section indices.<sup>54</sup> The diagonal elements of this object, where  $n$  equals  $m$ , represent the net charge change found on the  $m$ th cross-section subsequent to an electronic transition from the ground (G) to excited state ( $S_i$ ).<sup>55–57</sup> Projecting the diagonal elements of  $(\xi_{S_i})_{mn}$  in the basis of real-space orbitals allows for the visualization of the spatially resolved transition density. Additionally, to obtain a quantitative measure of the localization properties of the exciton, we computed the so-called participation ratio  $L_d$ ,

$$P_m = \frac{|\langle \xi_{S_i} \rangle_{mm}|}{\sum_k |\langle \xi_{S_i} \rangle_{kk}|} \quad (1)$$

$$L_d = \frac{1}{\sum_m P_m^2} \quad (2)$$

where the self-normalized diagonal elements  $P_m$  of the transition density matrix (for some transition to state  $S_i$  whose label is omitted for clarity) are used to define a probability distribution. To acquire a physical length, we multiply the width of each cross-section (0.5 Å in all cases) by the computed value  $1 < L_d < N$ , where  $N$  is the total number of cross-sections.

## ASSOCIATED CONTENT

### Supporting Information

The Supporting Information is available free of charge at <https://pubs.acs.org/doi/10.1021/acsnano.0c07544>.

Figures showing the effects of rose bengal concentration, guanine content, ssDNA length, tandem ssDNA sequences on SWCNT chemical functionalization, and the biexponential decay of defect-state PL; EVET mechanism and simulation details (PDF)

## AUTHOR INFORMATION

### Corresponding Authors

**Yu Zheng** – Center for Integrated Nanotechnologies, Materials Physics and Applications Division, Los Alamos National Laboratory, Los Alamos, New Mexico 87545, United States; [orcid.org/0000-0003-2703-9143](https://orcid.org/0000-0003-2703-9143); Email: [yzheng@lanl.gov](mailto:yzheng@lanl.gov)

**Han Htoon** – Center for Integrated Nanotechnologies, Materials Physics and Applications Division, Los Alamos National Laboratory, Los Alamos, New Mexico 87545,

United States; [orcid.org/0000-0003-3696-2896](https://orcid.org/0000-0003-3696-2896);  
Email: [htoon@lanl.gov](mailto:htoon@lanl.gov)

## Authors

**Braden M. Weight** – Center for Nonlinear Studies, Los Alamos National Laboratory, Los Alamos, New Mexico 87545, United States; Department of Physics, North Dakota State University, Fargo, North Dakota 58102, United States; [orcid.org/0000-0002-2441-3569](https://orcid.org/0000-0002-2441-3569)

**Andrew C. Jones** – Center for Integrated Nanotechnologies, Materials Physics and Applications Division, Los Alamos National Laboratory, Los Alamos, New Mexico 87545, United States; [orcid.org/0000-0001-9205-4847](https://orcid.org/0000-0001-9205-4847)

**Vigneshwaran Chandrasekaran** – Center for Integrated Nanotechnologies, Materials Physics and Applications Division, Los Alamos National Laboratory, Los Alamos, New Mexico 87545, United States; [orcid.org/0000-0002-6014-9953](https://orcid.org/0000-0002-6014-9953)

**Brendan J. Gifford** – Center for Nonlinear Studies, Los Alamos National Laboratory, Los Alamos, New Mexico 87545, United States; [orcid.org/0000-0002-4116-711X](https://orcid.org/0000-0002-4116-711X)

**Sergei Tretiak** – Center for Integrated Nanotechnologies, Materials Physics and Applications Division and Center for Nonlinear Studies, Los Alamos National Laboratory, Los Alamos, New Mexico 87545, United States; [orcid.org/0000-0001-5547-3647](https://orcid.org/0000-0001-5547-3647)

**Stephen K. Doorn** – Center for Integrated Nanotechnologies, Materials Physics and Applications Division, Los Alamos National Laboratory, Los Alamos, New Mexico 87545, United States; [orcid.org/0000-0002-9535-2062](https://orcid.org/0000-0002-9535-2062)

Complete contact information is available at:  
<https://pubs.acs.org/10.1021/acsnano.0c07544>

## Notes

The authors declare no competing financial interest.

## ACKNOWLEDGMENTS

This work was conducted at the Center for Integrated Nanotechnologies, a U.S. Department of Energy, Office of Basic Energy Sciences, user facility and supported mainly by DOE, BES, Quantum Information Science Infrastructure Development Project, Deterministic Placement and Integration of Quantum Defect. B.M.W. acknowledges the LANL institutional computing and NDSU's Center for Computationally Assisted Science and Technology (CCAST) for computational resources. We are grateful to Ali A. Alizadehmojarad for providing the molecular dynamics snapshot of ssDNA-SWCNTs.

## REFERENCES

- (1) Aguirre, C.; Auvray, S.; Pigeon, S.; Izquierdo, R.; Desjardins, P.; Martel, R. Carbon Nanotube Sheets As Electrodes In Organic Light-Emitting Diodes. *Appl. Phys. Lett.* **2006**, *88*, 183104.
- (2) Avouris, P.; Freitag, M.; Perebeinos, V. Carbon-Nanotube Photonics and Optoelectronics. *Nat. Photonics* **2008**, *2*, 341.
- (3) Mueller, T.; Kinoshita, M.; Steiner, M.; Perebeinos, V.; Bol, A. A.; Farmer, D. B.; Avouris, P. Efficient Narrow-Band Light Emission from A Single Carbon Nanotube p-n Diode. *Nat. Nanotechnol.* **2010**, *5*, 27.
- (4) Ma, X.; Hartmann, N. F.; Baldwin, J. K. S.; Doorn, S. K.; Htoon, H. Room-Temperature Single-Photon Generation from Solitary Dopants of Carbon Nanotubes. *Nat. Nanotechnol.* **2015**, *10*, 671.
- (5) He, X.; Hartmann, N. F.; Ma, X.; Kim, Y.; Ihly, R.; Blackburn, J. L.; Gao, W.; Kono, J.; Yomogida, Y.; Hirano, A.; Tanaka, T.; Kataura,

H.; Htoon, H.; Doorn, S. K. Tunable Room-Temperature Single-Photon Emission at Telecom Wavelengths from  $sp^3$  Defects In Carbon Nanotubes. *Nat. Photonics* **2017**, *11*, 577.

(6) Luo, Y.; He, X.; Kim, Y.; Blackburn, J. L.; Doorn, S. K.; Htoon, H.; Strauf, S. Carbon Nanotube Color Centers in Plasmonic Nanocavities: A Path to Photon Indistinguishability at Telecom Bands. *Nano Lett.* **2019**, *19*, 9037–9044.

(7) Ghosh, S.; Bachilo, S. M.; Simonette, R. A.; Beekingham, K. M.; Weisman, R. B. Oxygen Doping Modifies Near-Infrared Band Gaps in Fluorescent Single-Walled Carbon Nanotubes. *Science* **2010**, *330*, 1656–1659.

(8) Piao, Y.; Meany, B.; Powell, L. R.; Valley, N.; Kwon, H.; Schatz, G. C.; Wang, Y. Brightening of Carbon Nanotube Photoluminescence through the Incorporation of  $sp^3$  Defects. *Nat. Chem.* **2013**, *5*, 840.

(9) Lin, C.-W.; Bachilo, S. M.; Zheng, Y.; Tsedev, U.; Huang, S.; Weisman, R. B.; Belcher, A. M. Creating Fluorescent Quantum Defects in Carbon Nanotubes Using Hypochlorite and Light. *Nat. Commun.* **2019**, *10*, 2874.

(10) Zheng, Y.; Bachilo, S. M.; Weisman, R. B. Photoexcited Aromatic Reactants Give Multicolor Carbon Nanotube Fluorescence from Quantum Defects. *ACS Nano* **2020**, *14*, 715–723.

(11) Kwon, H.; Kim, M.; Meany, B.; Piao, Y.; Powell, L. R.; Wang, Y. Optical Probing of Local pH and Temperature in Complex Fluids with Covalently Functionalized, Semiconducting Carbon Nanotubes. *J. Phys. Chem. C* **2015**, *119*, 3733–3739.

(12) Shiraki, T.; Onitsuka, H.; Shiraishi, T.; Nakashima, N. Near Infrared Photoluminescence Modulation of Single-Walled Carbon Nanotubes Based on A Molecular Recognition Approach. *Chem. Commun.* **2016**, *52*, 12972–12975.

(13) Hartmann, N. F.; Yalcin, S. E.; Adamska, L.; Hároz, E. H.; Ma, X.; Tretiak, S.; Htoon, H.; Doorn, S. K. Photoluminescence Imaging of Solitary Dopant Sites in Covalently Doped Single-Wall Carbon Nanotubes. *Nanoscale* **2015**, *7*, 20521–20530.

(14) Danné, N.; Kim, M.; Godin, A. G.; Kwon, H.; Gao, Z.; Wu, X.; Hartmann, N. F.; Doorn, S. K.; Lounis, B.; Wang, Y. Ultrashort Carbon Nanotubes That Fluoresce Brightly in the Near-Infrared. *ACS Nano* **2018**, *12*, 6059–6065.

(15) Zheng, M.; Jagota, A.; Semke, E. D.; Diner, B. A.; McLean, R. S.; Lustig, S. R.; Richardson, R. E.; Tassi, N. G. DNA-Assisted Dispersion and Separation of Carbon Nanotubes. *Nat. Mater.* **2003**, *2*, 338–342.

(16) Zheng, M.; Jagota, A.; Strano, M. S.; Santos, A. P.; Barone, P.; Chou, S. G.; Diner, B. A.; Dresselhaus, M. S.; Mclean, R. S.; Onoa, G. B.; Samsonidze, G. G.; Semke, E. D.; Usrey, M.; Walls, D. J. Structure-Based Carbon Nanotube Sorting by Sequence-Dependent DNA Assembly. *Science* **2003**, *302*, 1545–1548.

(17) Zheng, Y.; Bachilo, S. M.; Weisman, R. B. Quenching of Single-Walled Carbon Nanotube Fluorescence by Dissolved Oxygen Reveals Selective Single-Stranded DNA Affinities. *J. Phys. Chem. Lett.* **2017**, *8*, 1952–1955.

(18) Zheng, Y.; Alizadehmojarad, A. A.; Bachilo, S. M.; Kolomeisky, A. B.; Weisman, R. B. Dye Quenching of Carbon Nanotube Fluorescence Reveals Structure-Selective Coating Coverage. *ACS Nano* **2020**, *14*, 12148–12158.

(19) Zheng, Y.; Bachilo, S. M.; Weisman, R. B. Controlled Patterning of Carbon Nanotube Energy Levels by Covalent DNA Functionalization. *ACS Nano* **2019**, *13*, 8222–8228.

(20) Perebeinos, V.; Tersoff, J.; Avouris, P. Radiative Lifetime of Excitons in Carbon Nanotubes. *Nano Lett.* **2005**, *5*, 2495–2499.

(21) Berciaud, S.; Cognet, L.; Lounis, B. Luminescence Decay and the Absorption Cross Section of Individual Single-Walled Carbon Nanotubes. *Phys. Rev. Lett.* **2008**, *101*, 077402.

(22) Miyauchi, Y.; Matsuda, K.; Yamamoto, Y.; Nakashima, N.; Kanemitsu, Y. Length-Dependent Photoluminescence Lifetimes in Single-Walled Carbon Nanotubes. *J. Phys. Chem. C* **2010**, *114*, 12905–12908.

(23) Harrah, D. M.; Swan, A. K. The Role of Length and Defects on Optical Quantum Efficiency and Exciton Decay Dynamics in Single-Walled Carbon Nanotubes. *ACS Nano* **2011**, *5*, 647–655.

- (24) Hartmann, N. F.; Velizhanin, K. A.; Haroz, E. H.; Kim, M.; Ma, X.; Wang, Y.; Htoon, H.; Doorn, S. K. Photoluminescence Dynamics of Aryl  $sp^3$  Defect States in Single-Walled Carbon Nanotubes. *ACS Nano* **2016**, *10*, 8355–8365.
- (25) He, X.; Velizhanin, K. A.; Bullard, G.; Bai, Y.; Olivier, J.-H.; Hartmann, N. F.; Gifford, B. J.; Kilina, S.; Tretiak, S.; Htoon, H.; Therien, M. J.; Doorn, S. K. Solvent- and Wavelength-Dependent Photoluminescence Relaxation Dynamics of Carbon Nanotube  $sp^3$  Defect States. *ACS Nano* **2018**, *12*, 8060–8070.
- (26) Perebeinos, V.; Avouris, P. Phonon and Electronic Non-radiative Decay Mechanisms of Excitons in Carbon Nanotubes. *Phys. Rev. Lett.* **2008**, *101*, 057401.
- (27) DeRosa, M. C.; Crutchley, R. J. Photosensitized Singlet Oxygen and Its Applications. *Coord. Chem. Rev.* **2002**, *233*, 351–371.
- (28) Zheng, Y.; Bachilo, S. M.; Weisman, R. B. Enantiomers of Single-Wall Carbon Nanotubes Show Distinct Coating Displacement Kinetics. *J. Phys. Chem. Lett.* **2018**, *9*, 3793–3797.
- (29) Saito, R.; Grüneis, A.; Samsonidze, G. G.; Brar, V.; Dresselhaus, G.; Dresselhaus, M.; Jorio, A.; Cançado, L.; Fantini, C.; Pimenta, M. Double Resonance Raman Spectroscopy of Single-Wall Carbon Nanotubes. *New J. Phys.* **2003**, *5*, 157.
- (30) Dresselhaus, M. S.; Jorio, A.; Hofmann, M.; Dresselhaus, G.; Saito, R. Perspectives on Carbon Nanotubes and Graphene Raman Spectroscopy. *Nano Lett.* **2010**, *10*, 751–758.
- (31) Miyata, Y.; Mizuno, K.; Kataura, H. Purity and Defect Characterization of Single-Wall Carbon Nanotubes Using Raman Spectroscopy. *J. Nanomater.* **2011**, *2011*, 1.
- (32) Cadet, J.; Ravanat, J. L.; Martinez, G. R.; Medeiros, M. H.; Mascio, P. D. Singlet Oxygen Oxidation of Isolated and Cellular DNA: Product Formation and Mechanistic Insights. *Photochem. Photobiol.* **2006**, *82*, 1219–1225.
- (33) Hayashida, T.; Umemura, K. Atomic Force Microscopy of DNA-Wrapped Single-walled Carbon Nanotubes in Aqueous Solution. *Colloids Surf., B* **2016**, *143*, 526–531.
- (34) Campbell, J. F.; Tessmer, I.; Thorp, H. H.; Erie, D. A. Atomic Force Microscopy Studies of DNA-Wrapped Carbon Nanotube Structure and Binding to Quantum Dots. *J. Am. Chem. Soc.* **2008**, *130*, 10648–10655.
- (35) Li, Z.; Song, Y.; Li, A.; Xu, W.; Zhang, W. Direct Observation of the Wrapping/Unwrapping of ssDNA around/from a SWCNT at the Single-Molecule Level: Towards Tuning The Binding Mode And Strength. *Nanoscale* **2018**, *10*, 18586–18596.
- (36) Chi, Q.; Wang, G.; Jiang, J. The Persistence Length and Length per Base of Single-Stranded DNA Obtained from Fluorescence Correlation Spectroscopy Measurements Using Mean Field Theory. *Phys. A* **2013**, *392*, 1072–1079.
- (37) Johnson, R. R.; Johnson, A. C.; Klein, M. L. Probing the Structure of DNA-Carbon Nanotube Hybrids with Molecular Dynamics. *Nano Lett.* **2008**, *8*, 69–75.
- (38) Zerze, G. H.; Stillinger, F. H.; Debenedetti, P. G. The Handedness of DNA Assembly around Carbon Nanotubes Is Determined by the Chirality of DNA. *J. Phys. Chem. B* **2020**, *124*, 5362–5369.
- (39) Kilina, S.; Tretiak, S. Excitonic and Vibrational Properties of Single-Walled Semiconducting Carbon Nanotubes. *Adv. Funct. Mater.* **2007**, *17*, 3405–3420.
- (40) Saha, A.; Gifford, B. J.; He, X.; Ao, G.; Zheng, M.; Kataura, H.; Htoon, H.; Kilina, S.; Tretiak, S.; Doorn, S. K. Narrow-Band Single-Photon Emission through Selective Aryl Functionalization of Zigzag Carbon Nanotubes. *Nat. Chem.* **2018**, *10*, 1089–1095.
- (41) He, X.; Gifford, B. J.; Hartmann, N. F.; Ihly, R.; Ma, X.; Kilina, S. V.; Luo, Y.; Shayan, K.; Strauf, S.; Blackburn, J. L.; Tretiak, S.; Doorn, S. K.; Htoon, H. Low-Temperature Single Carbon Nanotube Spectroscopy of  $sp^3$  Quantum Defects. *ACS Nano* **2017**, *11*, 10785–10796.
- (42) Gifford, B. J.; He, X.; Kim, M.; Kwon, H.; Saha, A.; Sifain, A. E.; Wang, Y.; Htoon, H.; Kilina, S.; Doorn, S. K.; Tretiak, S. Optical Effects of Divalent Functionalization of Carbon Nanotubes. *Chem. Mater.* **2019**, *31*, 6950–6961.
- (43) Kwon, H.; Furmanchuk, A. O.; Kim, M.; Meany, B.; Guo, Y.; Schatz, G. C.; Wang, Y. Molecularly Tunable Fluorescent Quantum Defects. *J. Am. Chem. Soc.* **2016**, *138*, 6878–6885.
- (44) Davydov, A. S. The Theory of Molecular Excitons. *Sov. Phys. Uspekhi* **1964**, *7*, 145.
- (45) Kasha, M. Energy Transfer Mechanisms and the Molecular Exciton Model for Molecular Aggregates. *Radiat. Res.* **1963**, *20*, 55–70.
- (46) Hochstrasser, R. M.; Kasha, M. Application of the Exciton Model to Mono-Molecular Lamellar Systems. *Photochem. Photobiol.* **1964**, *3*, 317–331.
- (47) Kasha, M.; Rawls, H. R.; El-Bayoumi, M. A. The Exciton Model in Molecular Spectroscopy. *Pure Appl. Chem.* **1965**, *11*, 371–392.
- (48) Sharma, A.; Gifford, B. J.; Kilina, S. Tip Functionalization of Finite Single-Walled Carbon Nanotubes and Its Impact on the Ground and Excited State Electronic Structure. *J. Phys. Chem. C* **2017**, *121*, 8601–8612.
- (49) Gifford, B. J.; Kilina, S.; Htoon, H.; Doorn, S. K.; Tretiak, S. Exciton Localization and Optical Emission in Aryl-Functionalized Carbon Nanotubes. *J. Phys. Chem. C* **2018**, *122*, 1828–1838.
- (50) Yanai, T.; Tew, D. P.; Handy, N. C. A New Hybrid Exchange-Correlation Functional Using the Coulomb-Attenuating Method (CAM-B3LYP). *Chem. Phys. Lett.* **2004**, *393*, 51–57.
- (51) Frisch, M.; Trucks, G.; Schlegel, H.; Scuseria, G.; Robb, M.; Cheeseman, J.; Scalmani, G.; Barone, V.; Petersson, G.; Nakatsuji, H. *Gaussian 16*; Gaussian, Inc.: Wallingford, CT, 2016.
- (52) Kohn, W.; Sham, L. J. Self-Consistent Equations Including Exchange and Correlation Effects. *Phys. Rev.* **1965**, *140*, A1133–A1138.
- (53) Casida, M. E.; Jamorski, C.; Casida, K. C.; Salahub, D. R. Molecular Excitation Energies to High-Lying Bound States from Time-Dependent Density-Functional Response Theory: Characterization and Correction of the Time-Dependent Local Density Approximation Ionization Threshold. *J. Chem. Phys.* **1998**, *108*, 4439–4449.
- (54) Lu, T.; Chen, F. Multiwfn: A Multifunctional Wavefunction Analyzer. *J. Comput. Chem.* **2012**, *33*, 580–592.
- (55) Luzanov, A.; Sukhorukov, A.; Umanskii, V. Application of Transition Density Matrix for Analysis of Excited States. *Theor. Exp. Chem.* **1976**, *10*, 354–361.
- (56) Mukamel, S.; Tretiak, S.; Wagersreiter, T.; Chernyak, V. Electronic Coherence and Collective Optical Excitations of Conjugated Molecules. *Science* **1997**, *277*, 781–787.
- (57) Tretiak, S.; Mukamel, S. Density Matrix Analysis and Simulation of Electronic Excitations in Conjugated and Aggregated Molecules. *Chem. Rev.* **2002**, *102*, 3171–3212.